ISSN 0021-3640, JETP Letters, 2010, Vol. 92, No. 6, pp. 396–400. © Pleiades Publishing, Inc., 2010.
Original Russian Text © B.B. Straumal, A.A. Myatiev, P.B. Straumal, A.A. Mazilkin, S.G. Protasova, E. Goering, B. Baretzky, 2010, published in Pis'ma v Zhurnal Éksperimental'noĭ i Teoreticheskoĭ Fiziki, 2010, Vol. 92, No. 6, pp. 438–443.

Grain Boundary Layers in Nanocrystalline Ferromagnetic Zinc Oxide

B. B. Straumal[a, b, d], A. A. Myatiev[b], P. B. Straumal[b, c], A. A. Mazilkin[a, d], S. G. Protasova[a, d], E. Goering[d], and B. Baretzky[e]

[a] *Institute of Solid State Physics, Russian Academy of Sciences, Chernogolovka, Moscow region, 142432 Russia*
e-mail: straumal@issp.ac.ru, straumal@mf.mpg.de
[b] *National University of Science and Technology MISIS, Leninskii pr. 4, Moscow, 119049 Russia*
[c] *Institut für Materialphysik, Universität Münster, 48149 Münster, Germany*
[d] *Max-Planck-Institut für Metallforschung, 70569 Stuttgart, Germany*
[e] *Karlsruher Institut für Technologie, Institut für Nanotechnologie, 76344 Eggenstein-Leopoldshafen, Germany*

Received August 3, 2010

The complete solubility of an impurity in a polycrystal increases with decreasing grain size, because the impurity dissolves not only in the crystallite bulk but also on the grain boundaries. This effect is especially strong when the adsorption layers (or the grain boundary phases) are multilayer. For example, the Mn solubility in the nanocrystalline films (where the size of grains is ~20 nm) is more than three times greater than that in the ZnO single crystals. The thin nanocrystalline Mn-doped ZnO films in the Mn concentration range 0.1–47 at % have been obtained from organic precursors (butanoates) by the "liquid ceramic" method. They have ferromagnetic properties, because the specific area of the grain boundaries in them is greater than the critical value [B.B. Straumal et al., Phys. Rev. B **79**, 205206 (2009)]. The high-resolution electron transmission microscopy studies show that the ZnO nanocrystalline grains with the wurtzite lattice are separated by amorphous layers whose thickness increases with the Mn concentration. The morphology of these layers differs greatly from the structure of the amorphous prewetting films on the grain boundaries in the ZnO:Bi_2O_3 system.

DOI: 10.1134/S0021364010180074

In 2000, Dietl et al. [1] were the first to predict theoretically that oxides (e.g., ZnO) doped with the "magnetic" atoms (e.g., Co, Mn, or Fe) might have ferromagnetic properties with the Curie temperature above room temperature. That study initiated many experimental works whose authors tried to reveal the predicted ferromagnetism. Some teams of researchers have found well reproducible ferromagnetism in ZnO, while other teams reliably proved its absence. In [2], it was demonstrated that the crucial point is the grain boundaries between the ZnO crystallites. Ferromagnetism is observed only if the grain boundary area in the unit volume of the material is greater than a certain critical value ($s_{th} = (2 \pm 4) \times 10^5$ m^2/m^3 for the Mn-doped ZnO and $s_{th} = (7 \pm 3) \times 10^7$ m^2/m^3 for pure ZnO). In other words, the grain boundaries form a kind of "grain boundary foam" in the ZnO polycrystals, which becomes ferromagnetic above a certain percolation threshold. Therefore, it would be interesting to determine the structure of the grain boundaries inducing ferromagnetism in ZnO.

The transparent oxide semiconductors with ferromagnetic properties are of interest for possible applications in spintronics. Of all the 3*d* elements, the Mn ions have the highest magnetic moment. The saturation magnetization in Mn-doped ZnO has a peculiar nonmonotonic dependence on the Mn concentration [3–18]. These facts can be attributed to a strong segregation of Mn on the grain boundaries in ZnO. It could even be expected that rather thick layers may appear on the grain boundary like the amorphous grain boundary phases in Bi-doped ZnO [19–24]. For this reason, the objective of this work is to investigate the grain boundary structures in nanocrystalline Mn-doped ZnO.

The thin nonporous nanocrystalline Mn-doped ZnO films were synthesized by the so-called "liquid ceramic" method [25]. The precursor was zinc butanoate (II) dissolved in an organic solvent to a zinc concentration of 1 to 4 kg/m^3. To prepare the doped films with the Mn concentration from 0.1 to 47 at %, zinc butanoate (II) and manganese butanoate (III) were mixed in the proper proportion. The precursor was deposited on the pure polycrystalline aluminum foil or on the sapphire single crystals with the (102) surface orientation. After 30 min of drying in air at 100°C, thermal pyrolysis at 550°C was performed in a resistance furnace in air. The Zn and Mn concentrations in the resulting films were measured using atomic adsorption spectroscopy in a Perkin–Elmer instrument and using the electron probe X-ray microanalysis (EPMA) on a Tescan Vega TS5130 MM scanning

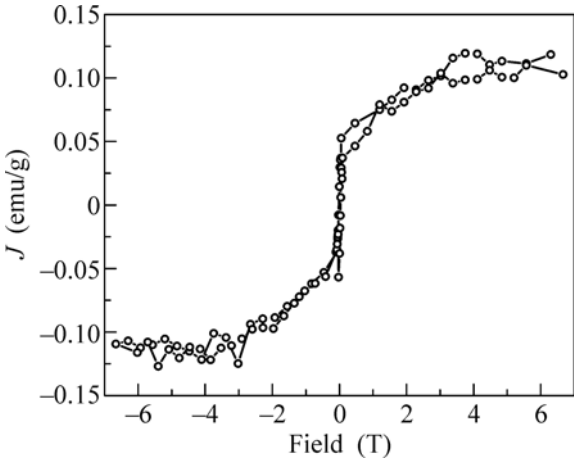

Fig. 1. Field dependence of the magnetization for the ZnO film with 13 at % Mn on the sapphire substrate.

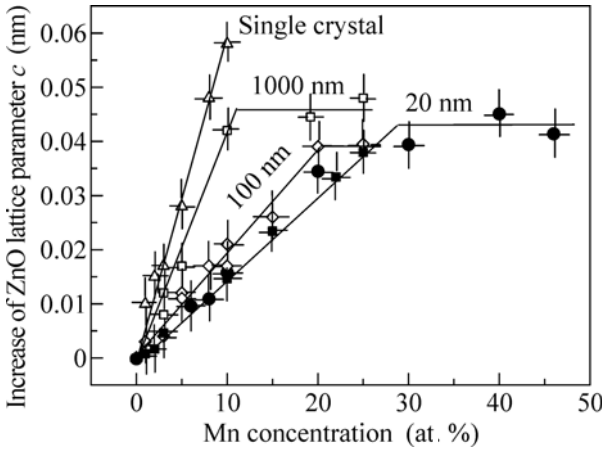

Fig. 2. Wurtzite lattice parameter c of ZnO versus the Mn concentration for different grain sizes. The triangles are the data for single crystals taken from [29]. The open squares and diamonds are the data for the polycrystals with a grain size of 1000 and 100 nm, respectively, taken from [30–32]. The closed circles and squares are the data for the lattice parameter in the ZnO films with a grain size of 20 nm taken from [33] and the measurements in this work and in [27], respectively.

microscope with an Oxford Instruments LINK energy dispersive spectrometer. The concentrations of the residual ferromagnetic impurities (Fe, Co, and Ni) did not exceed 0.001 at %. The films were transparent, occasionally with a greenish shade, from 50 to 900 nm thick. The film thickness was determined by EPMA and transmission electron microscopy (TEM) (on the transversal cuts). The TEM measurements were performed on a Joel JEM-4000FX electron microscope at an accelerating voltage of 400 kV. The X-ray diffraction was studied on a Siemens diffractometer using Fe Kα radiation. The grain size D was estimated in terms of the broadening of the X-ray diffraction peaks by the Scherrer formula $\beta = 0.9\lambda/D\cos\theta$, where λ is the X-ray wavelength, θ is the diffraction angle, and β is the FWHM of the diffraction line [26]. The magnetic properties of the films were measured on Quantum Design MPMS-7 and MPMS-XL SQUID magnetometers.

All the ZnO films studied had ferromagnetic properties. Figure 1 presents the magnetization curve for the ZnO film with 13 at % Mn on the sapphire substrate. Its shape is typical of a ferromagnetic material: the saturation at the applied fields higher than ~2 T and the coercive force of about 0.03 T. The saturation magnetization of the films is a nonmonotonic function of the Mn concentration in the range of 0.01–0.16 emu/g [18].

Figure 2 presents the period of the ZnO wurtzite lattice as a function of the Mn concentration for different grain sizes. The lattice period increases as manganese is added. When the limit of Mn solubility in the matrix is reached, the ZnO lattice period ceases to increase, and the lines of cubic manganese oxide, Mn_3O_4, appear in the X-ray [27] and electron diffraction patterns (see Fig. 3). In the single crystals, the solubility limit is reached at 10 at % Mn. In the polycrystals, the added Mn atoms are arranged both in the bulk being substituted for the Zn atoms in the wurtzite lattice and in the (looser packed) grain boundaries. The adsorption capacity of the grain boundaries is rather high [28], and thus the total Mn solubility increases as

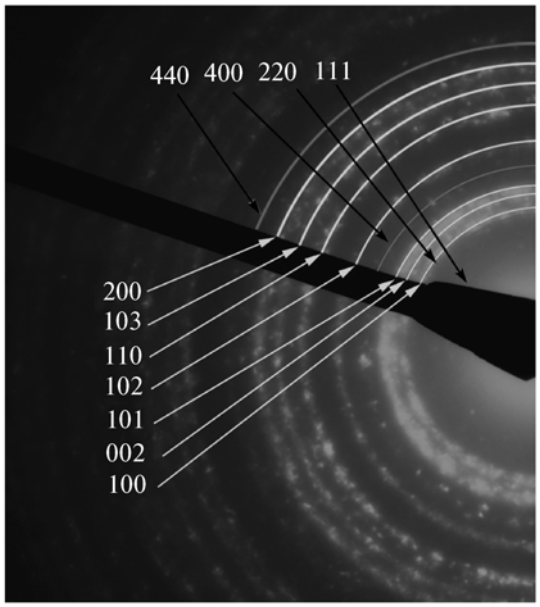

Fig. 3. Electron diffraction pattern for the ZnO sample with 30 at % Mn. The indices for the strong lines of the ZnO wurtzite lattice are given in the column on the left. The indices of the weak lines of the manganese oxide particles are given in the upper line.

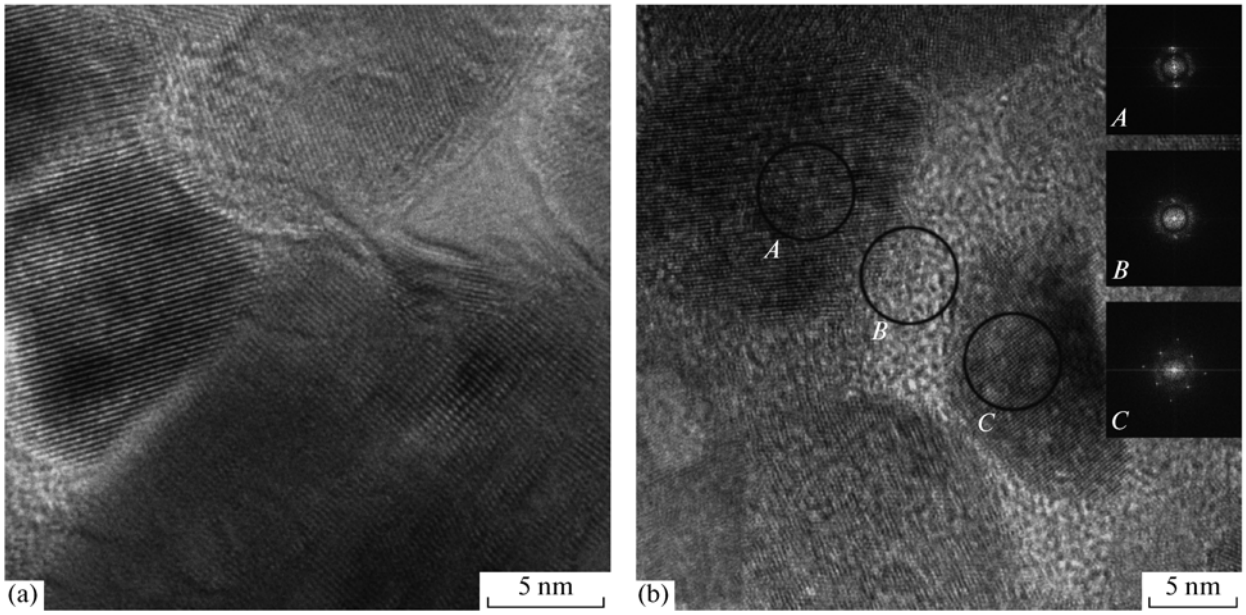

Fig. 4. Bright-field high-resolution transmission electron micrographs of the doped ZnO films (a) with 10 at % Mn, amorphous layers between ZnO nanocrystalline grains are seen; and (b) with 15 at % Mn, ZnO nanocrystalline grains are surrounded by amorphous layers. The insets show the Fourier transform patterns for the amorphous and crystalline regions.

compared to that in the single crystal. The finer the grains (or more boundaries in the unit volume), the greater the increase in the total solubility (see Fig. 2). For example, it is 20 and 30 at % Mn for at a grain size of 100 and 20 nm, respectively. The maximum solubility in the bulk does not depend on the grain size and, therefore, at a grain size of 20 nm, only one third of the Mn atoms are dissolved in the bulk, while two thirds of the Mn atoms are dissolved at the intergrain boundaries.

What is the structure of these boundaries, and where are two thirds of manganese atoms dissolved in the polycrystal hidden? Figure 4 presents the bright field micrographs of the Mn-doped ZnO films with (a) 10 and (b) 15 at % Mn obtained using high-resolution transmission electron microscopy (HRTEM). The direct resolution of the lattice makes it possible to see the crystalline ZnO grains with the wurtzite lattice. It is clearly seen in Fig. 4a that the amorphous phase layers are at the boundaries between these grains. As the Mn concentration increases from 10 to 15 at %, the amorphous phase fraction increases. It is readily illustrated by the comparison of the structures shown in Figs. 4a and 4b. For example, one of the ZnO grains with the wurtzite lattice (at the center) in Fig. 4b is surrounded by the Mn-enriched amorphous region. Since the amorphous layers in the sample with 15 at % Mn are already rather large, it is possible to obtain the patterns of the Fourier transforms for the amorphous and crystalline regions. In Fig. 4b, letters A, B, and C denote the relevant crystalline grains (on the left and right) and the amorphous layer (in the middle).

Figure 4 illustrates the situation occurring when manganese is gradually added to nanocrystalline ZnO. In the doping process, some Mn atoms come into the crystal lattice of the grains and contribute to the displacements of X-ray diffraction peaks from the coherent scattering regions (the wurtzite lattice grains). The remaining Mn atoms (about two thirds) come to the amorphous layers, which surround and separate the grains. These amorphous layers become thicker with an increase in the Mn concentration. Our earlier quantitative estimate demonstrates that at 30 at % Mn, when the solubility limit is reached for the 20-nm grains, the thickness of the grain boundary layers is 6–10 ML of MnO, while it is 2 ML on the outer surface [27]. This situation differs radically from the monolayer McLean adsorption (on the surface or on the grain boundary) [34]. The amorphous layers of the grain boundary phase of a constant thickness of several nanometers were first observed and theoretically described in the force balance model in the pioneering works concerning silicon nitride [35, 36]. Later on, noncrystalline layers of a constant (or equilibrium) thickness of several nanometers were repeatedly observed in ceramic materials [19–24] or at the metal/oxide interfaces [37, 38]. The thin equilibrium layers appearing in the single-phase region of the phase diagram on the grain boundaries or outer surfaces were analyzed by Cahn [39]. He suggested that the transition from incomplete wetting of the outer surface to its complete wetting is a phase transformation. Then, this idea was successfully applied to the grain boundaries, and the data then existed on the

grain boundary wetting were revised in the light of these new considerations [40–42]. The grain boundary wetting phase transition occurs at a certain temperature T_{wGB} at which the grain boundary energy σ_{GB} becomes equal to the double energy of the interface between the solid and liquid phases $2\sigma_{SL}$. Above T_{wGB}, the grain boundary is replaced by a liquid phase layer. As a result, the conode of the grain boundary wetting phase transition appears at T_{wGB} in the two-phase "solid phase + melt" region of the phase diagram. This conode continues in the single-phase "solid solution" region of the phase diagram as the grain boundary solidus line (or the prewetting transition line). The grain boundary contains a layer of the quasiliquid grain boundary phase between the bulk and grain boundary solidus lines. Above the temperature T_{wGB}, the energy gain from complete wetting ($\sigma_{GB} - 2\sigma_{SL}$) makes it possible to stabilize this quasi-liquid layer of the grain boundary phase. The formation of the metastable liquid phase layer of thickness l on the grain boundary requires the energy $l\Delta g$. The finite thickness l of the grain boundary phase is determined by the equality of the energy gain ($\sigma_{GB} - 2\sigma_{SL}$) from complete wetting and the energy loss $l\Delta g$ from the metastable liquid phase formation. In this simplest model, the liquid-like phase layer of thickness l appears on the grain boundary at the intersection of the prewetting line (the grain boundary solidus) $c_{bt}(T)$. The thickness l increases as a logarithmic function as the bulk solidus line is approached. This is because the "true" bulk liquid phase appears behind the bulk solidus line, and its thickness becomes thermodynamically infinite. In the two-phase "solid phase + melt" region of the phase diagram, the thickness of the liquid phase on the grain boundary is solely determined by its amount. Grain boundary layers with a thickness of several monolayers having anomalously high diffusion penetrability for solids were observed in the systems Cu–Bi [43], Al–Zn [44, 45], Fe–Si–Zn [46], and W–Ni [47].

However, the morphology of the Mn-enriched amorphous regions between the ZnO grains differs greatly from that of very homogeneous and uniformly thin amorphous layers of the prewetting grain boundary phases in the $ZnO:Bi_2O_3$ samples prepared by liquid-phase sintering [19–24]. For example, in a sample with 15 at % Mn (see Fig. 4b), the amorphous regions completely enclose some ZnO grains and only partially penetrate between the others. This microstructure is similar to the morphology of the two-phase polycrystals, where the second phase completely wets some boundaries and only partially wets other boundaries [40–42, 48, 49]. We have recently shown that the second (wetting) phase can be not only liquid but also solid [50–52]. At first sight, the structures revealed in Mn-doped ZnO (see Fig. 4) indicate that the second, amorphous phase can also wet the grain boundaries. However, this is not the case. In the conventional case, the wetting of the grain boundary in one phase by the other phase layers occurs in the two-phase region of the bulk phase diagram. Here, the composition of every phase is fixed and does not change with the component concentrations. In our case, as the Mn concentration increases, it does not remain constant in the matrix crystallites but also increases (see Fig. 2). At the Mn concentration above 30 at %, the second bulk phase of Mn_3O_4 appears (see Fig. 3). This means that the amorphous layers in Fig. 4 are not the true bulk phase but the grain boundary phase whose morphology has not been earlier observed.

To summarize, we have experimentally investigated the structures of the grain boundaries in doped ZnO, which form the grain boundary foam and are responsible for the magnetic properties arising in ZnO. The amorphous layers, which do not contribute to the displacement of the X-ray diffraction peaks from the coherent scattering regions (the wurtzite lattice grains), have been observed on the boundaries. As a result, at a grain size of 20 nm, only a third of the doping Mn atoms are built into the crystallite wurtzite lattice, while about two thirds of them come into the amorphous layers surrounding the grains.

We are grateful to A.N. Nekrasov for assistance in the experiments and to Prof. A.M. Gusak and P. van Aken for useful discussions. The work was supported by the Russian Foundation for Basic Research (project nos. 10-02-00086 and 09-08-90406), the National University of Science and Technology MISIS (program of creation and development), and the State Foundation for Basic Research of Ukraine (project no. X28.7049).

REFERENCES

1. T. Dietl, H. Ohno, F. Matsukura, et al., Science **287**, 1019 (2000).
2. B. B. Straumal, A. A. Mazilkin, S. G. Protasova, et al., Phys. Rev. B **79**, 205206 (2009).
3. S. K. Mandal, A. K. Das, T. K. Nath, et al., J. Appl. Phys. **100**, 104315 (2006).
4. S. Venkataraj, N. Ohashi, I. Sakaguchi, et al., J. Appl. Phys. **102**, 014905 (2007).
5. J. Alaria, P. Turek, M. Bernard, et al., Chem. Phys. Lett. **415**, 337 (2005).
6. S. Kolesnik and B. Dabrowski, J. Appl. Phys. **96**, 5379 (2004).
7. M. H. Kane, W. E. Fenwick, M. Strassburg, et al., Phys. Status Solidi B **244**, 1462 (2007).
8. A. I. Savchuk, P. N. Gorley, V. V. Khomyak, et al., Mater. Sci. Eng. B **109**, 196 (2004).
9. G. Lawes, A. S. Risbud, A. P. Ramirez, et al., Phys. Rev. B **71**, 045201 (2005).
10. O. D. Jayakumar, H. G. Salunke, R. M. Kadam, et al., Nanotechnology **17**, 1278 (2006).
11. M. Pal, Jpn. J. Appl. Phys. **44**, 7901 (2005).
12. B. Babič-Stojič, D. Milivojevič, J. Blanusa, et al., J. Phys.: Condens. Matter **20**, 235217 (2008).

13. Z. Yan, Y. Ma, D. Wang, et al., Appl. Phys. Lett. **92**, 081911 (2008).
14. M. Diaconu, H. Schmidt, H. Hochmuth, et al., J. Magn. Magn. Mater. **307**, 212 (2006).
15. M. Diaconu, H. Schmidt, H. Hochmuth, et al., Thin Solid Films **486**, 117 (2005).
16. Q. Xu, H. Schmidt, S. Zhou, et al., Appl. Phys. Lett. **92**, 082508 (2008).
17. N. Gopalakrishnan, J. Elanchezhiyan, K. P. Bhuvana, et al., Scr. Mater. **58**, 930 (2008).
18. B. B. Straumal, S. G. Protasova, A. A. Mazilkin, et al., J. Appl. Phys. **108**, 073923 (2010).
19. H. Wang and Y.-M. Chiang, J. Am. Ceram. Soc. **81**, 89 (1998).
20. J. P. Gambino, W. D. Kingery, G. E. Pike, et al., J. Am. Ceram. Soc. **72**, 642 (1989).
21. E. Olsson and G. L. Dunlop, J. Appl. Phys. **66**, 3666 (1989).
22. B. B. Straumal, A. A. Mazilkin, P. B. Straumal, et al., Int. J. Nanomanufact. **2**, 253 (2008).
23. J. Luo and Y.-M. Chiang, Ann. Rev. Mater. Res. **38**, 227 (2008).
24. H. Qian, J. Luo, and Y.-M. Chiang, Acta Mater. **56**, 862 (2008).
25. B. B. Straumal, A. A. Mazilkin, S. G. Protasova, et al., Acta Mater. **56**, 6246 (2008).
26. L. Lábár, Microsc. Microanal. **14**, 287 (2008).
27. B. B. Straumal, B. Baretzky, A. A. Mazilkin, et al., J. Eur. Ceram. Soc. **29**, 1963 (2009).
28. B. B. Straumal, *Grain Boundary Phase Transitions* (Nauka, Moscow, 2003) [in Russian].
29. K. Masuko, A. Ashida, T. Yoshimura, et al., J. Magn. Magn. Mater. **310**, E711 (2007).
30. A. C. Mofor, A. El-Shaer, A. Bakin, et al., Superlatt. Microstruc. **39**, 381 (2006).
31. L. R. Reddy, P. Prathap, Y. P. V. Subbaiah, et al., Solid State Sci. **9**, 718 (2007).
32. M. Yuan, W. Fu, H. Yang, et al., Mater. Lett. **63**, 1574 (2009).
33. H. Saal, M. Binnewies, M. Schrader, et al., Chem. Eur. J. **15**, 6408 (2009).
34. D. McLean, *Grain Boundaries in Metals* (Clarendon, Oxford, 1957).
35. D. R. Clarke, J. Am. Ceram. Soc. **70**, 15 (1987).
36. M. Bobeth, D. R. Clarke, and W. Pompe, J. Am. Ceram. Soc. **82**, 1537 (1999).
37. A. Avishai, C. Scheu, and W. D. Kaplan, Acta Mater. **53**, 1559 (2005).
38. M. Baram and W. D. Kaplan, J. Mater. Sci. **41**, 7775 (2006).
39. J. W. Cahn, J. Chem. Phys. **66**, 3667 (1977).
40. N. Eustathopoulos, Int. Met. Rev. **28**, 189 (1983).
41. B. Straumal, T. Muschik, W. Gust, et al., Acta Metall. Mater. **40**, 939 (1992).
42. B. Straumal, D. Molodov, and W. Gust, J. Phase Equilibria **15**, 386 (1994).
43. S. V. Divinski, M. Lohmann, Chr. Herzig, et al., Phys. Rev. B **71**, 104104 (2005).
44. B. B. Straumal, A. A. Mazilkin, O. A. Kogtenkova, et al., Phil. Mag. Lett. **87**, 423 (2007).
45. B. Straumal, R. Valiev, O. Kogtenkova, et al., Acta Mater **56**, 6123 (2008).
46. B. Straumal, E. Rabkin, W. Lojkowski, et al., Acta mater **45**, 1931 (1997).
47. J. Luo, V. K. Gupta, D. H. Yoon, et al., Appl. Phys. Lett. **87**, 231902 (2005).
48. B. B. Straumal, B. S. Bokstein, A. B. Straumal, et al., Pis'ma Zh. Eksp. Teor. Fiz. **88**, 615 (2008) [JETP Lett. **88**, 537 (2008)].
49. V. V. Belousov, JETP Lett. **88**, 297 (2008).
50. G. A. López, E. J. Mittemeijer, and B. B. Straumal, Acta Mater. **52**, 4537 (2004).
51. B. B. Straumal, B. Baretzky, O. A. Kogtenkova, et al., J. Mater. Sci. **45**, 2057 (2010).
52. B. B. Straumal, O. A. Kogtenkova, A. B. Straumal, et al., J. Mater. Sci. **45**, 4271 (2010).

Translated by E. Perova